Energy & Environmental Science

Atomically Dispersed Single Ni Site Catalysts for High-Efficiency CO2 Electroreduction at Industrial-Level Current Densities

Journal:	*Energy & Environmental Science*
Manuscript ID	EE-ART-01-2022-000318.R1
Article Type:	Paper
Date Submitted by the Author:	23-Mar-2022

Complete List of Authors:	Li, Yi; University at Buffalo - The State University of New York, Department of Chemical and Biological Engineering; Jiangsu University, School of Materials Science and Engineering Adli, Nadia; University at Buffalo Shan, Weitao; University of Pittsburgh, Department of Mechanical Engineering and Materials Science Wang, Maoyu; Oregon State University, Chemical, Biological, and Environmental Engineering Zachman, Michael; Oak Ridge National Laboratory Hwang, Sooyeon; Brookhaven National Laboratory, Center for Functional Nanomaterials Tabassum, Hassina ; University at Buffalo, Chemical and Biological Engineering Karakalos, Stavros; University of South Carolina, College of Engineering and Computing Feng, Zhenxing; Oregon State University, School of Chemical, Biological, and Environmental Engineering; Wang, Guofeng; University of Pittsburgh, Mechanical Engineering and Materials Science Li, Chris; University at Buffalo, Chemistry Wu, Gang; University at Buffalo, Chemical and Biological Engineering

Broader Context

Electrochemical carbon dioxide reduction reaction (CO_2RR) is a promising strategy to store renewable solar and wind energy in carbon-based fuels and chemicals, reducing anthropogenic CO_2 emissions. However, current electrocatalytic CO_2 reduction processes are inefficient due to the highly stable chemical bond in CO_2 and the competing water reduction reaction. Compared to other CO_2 reduction pathways, the reduction of CO_2 to CO represents one of the most practical pathways because of their easily achieved high selectivity (>90%) and large current densities. Nevertheless, the most efficient CO2 to CO conversion catalysts are based on precious metals such as Au and Ag, therefore, significantly hindering the large-scale application of the envisioned technology. This work reports a high-performance atomically dispersed single Ni site catalyst, which exhibited high-efficient CO_2 reduction to CO at an industrial-level current density in a flow cell. Also, extensive experimental and theoretical studies comprehensively elucidated the fundamental intrinsic and external factors concerning their effects on catalytic activity and selectivity of the single Ni site catalysts. The new catalyst technology could shed light on the CO generation from electrochemical CO_2 reduction using earth-abundant materials at the potential industrial scale.

Atomically Dispersed Single Ni Site Catalysts for High-Efficiency CO_2 Electroreduction at Industrial-Level Current Densities

Yi Li,[1, 2, Δ] Nadia Mohd Adli,[1, Δ] Weitao Shan,[3, Δ] Maoyu Wang,[4, Δ] Michael J. Zachman,[5] Sooyeon Hwang,[6] Hassina Tabassum,[1] Stavros Karakalos,[7] Zhenxing Feng,[4, *] Guofeng Wang,[3, *] Yuguang C. Li,[8, *] and Gang Wu[1,*]

[1]Department of Chemical and Biological Engineering, University at Buffalo, The State University of New York, Buffalo, New York 14260, United States

[2]School of Materials Science and Engineering, Jiangsu University, Zhenjiang, 212013, China

[3]Department of Mechanical Engineering and Materials Science, University of Pittsburgh, Pittsburgh, Pennsylvania 15261, United States

[4]School of Chemical Biological and Environmental Engineering, Oregon State University, Corvallis, OR 97331, United States

[5]Center for Nanophase Materials Sciences, Oak Ridge National Laboratory, Oak Ridge, TN, 37831 United States

[6]Center for Functional Nanomaterials, Brookhaven National Laboratory, Upton, NY 11973, United States

[7]Department of Chemical Engineering, University of South Carolina, Columbia, SC 29208, United States

[8]Department of Chemistry, University at Buffalo, The State University of New York, Buffalo, New York 14260, United States

Corresponding Authors: zhenxing.feng@oregonstate.edu (Z. Feng), guw8@pitt.edu (G. Wang); yuguangl@buffalo.edu (Y. Li), gangwu@buffalo.edu (G. Wu)

[Δ]These authors contributed equally.

Abstract: Atomically dispersed and nitrogen-coordinated single Ni sites (*i.e.*, NiN_x moieties) embedded in partially graphitized carbon have emerged as effective catalysts for CO_2 electroreduction to CO. However, much mystery remains behind the extrinsic and intrinsic factors that govern the overall catalytic CO_2 electrolysis performance. Here, we designed a high-performance single Ni site catalyst by systematically elucidating the structural evolution of NiN_x sites during thermal activation and other critical external factors (*e.g.*, carbon particle sizes and Ni content) based on Ni-N-C model catalysts derived from well-defined nitrogen-doped carbon carbonized from zeolitic imidazolate framework (ZIF)-8. The N coordination, metal-N bond length, and thermal wrinkling of carbon planes in Ni-N-C catalysts significantly depend on thermal temperatures. Density functional theory (DFT) calculations reveal that the shortening Ni-N bonds in compressively strained NiN_4 sites could intrinsically enhance the CO_2RR activity and selectivity in the Ni-N-C catalyst. Notably, the NiN_3 active sites formed at higher temperatures (e.g., 1200°C) is intrinsically more active than NiN_4, providing a new opportunity to design a highly active catalyst via stabilizing NiN_3 sites with increased density. We also studied how morphological factors such as the carbon host particle size and Ni loading alter the final catalyst's structure and performance. Notably, the implementation of this catalyst in an industrial flow-cell electrolyzer demonstrated an impressive performance for CO generation, achieving a current density of CO up to 726 mA cm^{-2} with Faradaic efficiency of CO above 90%, representing one of the best catalysts for CO_2 reduction to CO.

Keywords: Single metal sites; Ni-N-C catalyst; coordination structure; CO_2 reduction reaction; flow cells.

1. Introduction

The worldwide net gain of CO_2 in the atmosphere, which comprises roughly 65% of the greenhouse gas, is estimated to be over 20 billion metric tons every year and fast increasing.[1, 2] While the development of sustainable and clean energy technologies are actively being pursued, the progress is slow. Fossil fuels will likely remain dominant in sustaining the world's energy needs in the near future. Thus, viable solutions are desperately required to capture, store, and convert CO_2 inevitably produced from traditional fossil energy. Among exploring strategies, electrochemical carbon dioxide reduction reaction (CO_2RR) presents an effective way to convert CO_2 and create feedstocks, such as CO, for the Fischer-Tropsch reactions.[3, 4]

The CO_2RRs are thermodynamically feasible with standard potentials close to 0 V *vs.* RHE for most of its derivatives.[5] However, the reductive potential region for the CO_2RR overlaps with the hydrogen evolution reaction (HER), which takes place at 0 V and is kinetically more favorable on various transition metals. Furthermore, one of the primary intermediates during the CO_2RR is the CO_2^- radical, formed via an electron transfer to the CO_2 molecule. It is in an unstable structure requiring considerable activation energy. Therefore, identifying a highly selective and active catalyst for the CO_2RR is essential to realizing a viable CO_2 conversion to value-added chemicals at an industrial level. Among the possible CO_2RR products, CO is highly desirable due to the following reasons: (1) it requires a lower overpotential and fewer number of electrons to produce CO than other products such as ethylene and ethanol, thus resulting in a lower cost in practical applications; (2) CO itself is a feedstock for a variety of valuable chemicals such as aldehydes; (3) syngas, the combination of CO and H_2 at a proper ratio (when H_2 is produced from the HER as a by-product), is a valuable feedstock to produce liquid fuels through the Fischer-Tropsch (F-T) reactions.[6, 10] At present, precious metals are the only catalysts (*e.g.*, Au and Ag) that have been

shown to have good electrocatalytic performance with high Faradaic efficiencies (FEs) for CO generation.[7, 8] However, in order to develop the large-scale application of the envisioned technology, the cost of the precious metals these electrocatalysts will be prohibitively high. Non-precious metals such as Cu, Sn and Co have also been demonstrated for the CO_2RR; however, the stability of those catalysts remains a challenge.[9, 10] Furthermore, the most promising Cu-based catalysts mainly produce hydrocarbons in complex mixtures of C1, C2, and C3 products and require large negative overpotentials.[9, 11] Thus, selective production of CO on Cu-based catalysts is not favored. It has been a grand challenge in CO_2RR to have an ultrahigh (>95%) selectivity of any single product to minimize the separation cost for downstream applications.[5]

In recent years, heteroatom (non-precious metals, nitrogen)-doped carbon has emerged as a new class of promising electrocatalysts for various electrochemical reactions due to active metal sites' unique electronic and geometric structures, low-cost and earth-abundant nature.[12-21] In particular, the key to realizing a high selectivity from the CO_2RR to CO over the parasitic HER is to design single metal site catalysts (M: Fe, Co, Ni, and Mn), which are coordinated with N ligands and embedded in carbon planes (denoted thereon as M-N-C).[22] The unique electronic structure of the M-N_x sites strongly favors the binding of CO_2 molecules.[23-25] An ideal catalyst for the CO2RR should generate high j_{CO} with a decrease of potentials while maintaining high CO selectivity, *i.e.*, high $FE_{CO.}$ Fe sites are active at relatively positive potentials among studied single metal site catalysts while less selective to CO at low potentials. They also suffer from activity degradation due to the possible dementallation.[26, 27] On the contrary, single Ni sites are highly selective for CO, but less active at high potential due to their weak binding of the adsorbed CO.[28]

Regarding the intrinsic nature of Ni-N-C, several questions remain, such as the optimal coordination environment and configuration moieties for the CO_2RR. The primary debate focus

on the active site structures, including the saturated MN_4, the unsaturated ones, or defect-rich M-N_{4-x} (e.g., Ni-N_1-C[29], Ni-N_2-C[30, 31], Ni-N_3-C[32-35], and Ni-N_4-C[28, 36]). Two possible CO_2RR pathways are dependent on the coordination state, either the COOH* or the HCOO* pathways.[37] These riddles further necessitate a fundamental study focusing on the nature of the intrinsically active Ni-N_x-C moieties. Thus, understanding the intrinsic architecture of the Ni-N_x sites, particularly the coordination environment and how the Ni-N_x strain originating from the thermal wrinkling behavior of graphene dictates its CO_2RR performance, is meaningful and in high demand. However, one common hindrance in investigating the nature of the active sites of Ni-N-C catalysts is the convolution of the morphological and structural aspects of the carbon host with the intrinsic development of the active sites associated with the Ni-N bonds. Recently, we developed a unique two-step approach to design a well-defined model system to accurately control the carbon structures/morphologies, metal content, and M-N bonding structures.[3] Typically, a well-defined nitrogen-doped carbon host with controlled morphologies (surface areas, porosity, nitrogen dopants) can be derived from the ZIF-8 precursor at the first step. Then controlled Ni-N bonds can be generated by introducing Ni ions into the N-doped carbon host via chemical adsorption followed by thermal activation at different temperatures. This approach can deconvolute the complex processes involving carbonization, nitrogen doping, and M-N bond formation. Thus, the evolution of the Ni-N bonding structures associated with the intrinsic catalytic properties can be exclusively controlled by thermal activation temperature, which directly correlates with measured activity and selectivity toward the CO_2RR. The synthetic method reported in this study can increase the active single metal site content to ca. 2.2 wt% of Ni doping, significantly higher than the typical 1.0 wt% for a conventional Ni-N-C.[30] Consequently, the optimized single Ni site catalysts reported in this study can achieve a remarkable catalytic

performance approaching 92.0% FE of CO at 92.3 mA cm^{-2} and –0.9 V *vs.* RHE in a traditional H-cell configuration. Furthermore, the Ni-N-C catalyst demonstrated exceptional performance in an industrial CO_2 electrolyzer prototype, achieving 90.8% of FE for the CO generation at a high current density of 726 mA cm^{-2}.

2. Results and discussion

2.1 Catalyst synthesis and structures

The synthesis scheme to prepare Ni-N-C catalysts is highlighted in Figure 1a, which was modified from our previous works about Fe-N-C catalysts for the oxygen reduction reaction.[3] Briefly, ZIF-8 nanocrystals were prepared using $Zn(NO_3)_2$ and 2-methylimidazole ligands in a methanol solution. XRD patterns confirmed the well-defined ZIF-8 crystals featured with representative (110) and (100) planes (Figure S1).[38] High microporosity (inferred from the type IV isotherm of the N_2 adsorption/desorption isotherms) and mesoporosity characteristic of the pristine ZIF-8 were evidenced from the N_2 adsorption/desorption analysis at 77 K by using the BET method (Figure S2), showing a surface area surpassing 1500 m^2 g^{-1}. The pyrolysis of the ZIF-8 crystals at high temperatures (*i.e.*, 1100 °C) yielded an N-doped carbon structure (Figure S3) that shows hierarchical microporosity prime for hosting Ni(II) ions. Through tuning zinc salt concentration during the ZIF-8 synthesis, a wide range of sizes can be controlled for the ZIF-8 nanocrystal precursors (40 to 2000 nm), which were retained in the derived carbon hosts through one-step carbonization (Figure S4 and S5).

The samples were then washed with methanol after doping with Ni(II) ion precursors via a double-solvent approach by combining polar and non-polar media. After being dried under vacuum, they were subjected to a heat-treatment at various temperatures ranging from 400 to 1200°C. Despite the different heating temperatures, Ni ion loadings, and carbon host sizes, almost

identical graphitic carbon structures with broad reflections at 24.3° and 43.7° were observed without apparent metallic or oxides (Figure S3 and S6a). The Raman spectra in Figure S6b reveal a defect-rich carbon structure with prominent disordered D band and graphitic G band at ~1340 and ~1585 cm^{-1}, respectively, for all the Ni-N-C samples from the different thermal activation temperatures. The highest temperature studied, 1200°C, leads to slightly enhanced graphitization relative to other samples. Thus, based on the XRD and Raman results for the Ni-N-C samples thermally activated at different temperatures, the carbon structures of these materials are almost identical, allowing to exclusively study the evolving Ni-N_x site structures depending on thermal activations. In particular, an optimal Ni-N-C catalyst (e.g., 900 °C) was characterized by advanced electron microscopy techniques, including dark and bright-field scanning transmission electron microscopy (BF-STEM), and high-angle annular dark-field (HAADF)-STEM, and carbon K-edge EELS orientational mapping by multivariate curve resolution (MCR) (Figures 1b). Thus, the catalyst's overall carbon particle morphology and nanostructure and the presence of atomically dispersed single metal sites were comprehensively studied. In addition to 900 °C. The catalyst from 1200 °C is essential due to its enhanced intrinsic activity and selectivity but with overall low mass activity. Thus, Figure 1c further demonstrated its carbon nanostructures and atomic Ni site dispersion, similar to the catalyst from 900 °C. Therefore, the measured difference in catalytic properties is likely due to the changes in coordination environments and local structures at the atomic level, which was further elucidated later.

Figures S7 present the N_2 adsorption/desorption isotherms and pore size distributions for the Ni-N-C catalysts from different thermal activation temperatures. Compared to the Ni-free N-C sample, a striking loss of pores and surface area of the thermally activated Ni-N-C indicates that significant micropore volume was decreased after introducing active Ni sites.[39] With thermal

activation at 400 °C, the surface area is decreased due to the Ostwald-ripening process congregating the adsorbed ions into more stable small nanoparticles. Our previous understanding suggests that these metal nanoparticles can be thermally converted into atomically-dispersed active single metal sites due to the strong Lewis-base interaction between the cationic transition metal and the nucleophilic N-sites,[3, 27, 40, 41] which further explains the increased surface area of the sample treated at 900 °C.

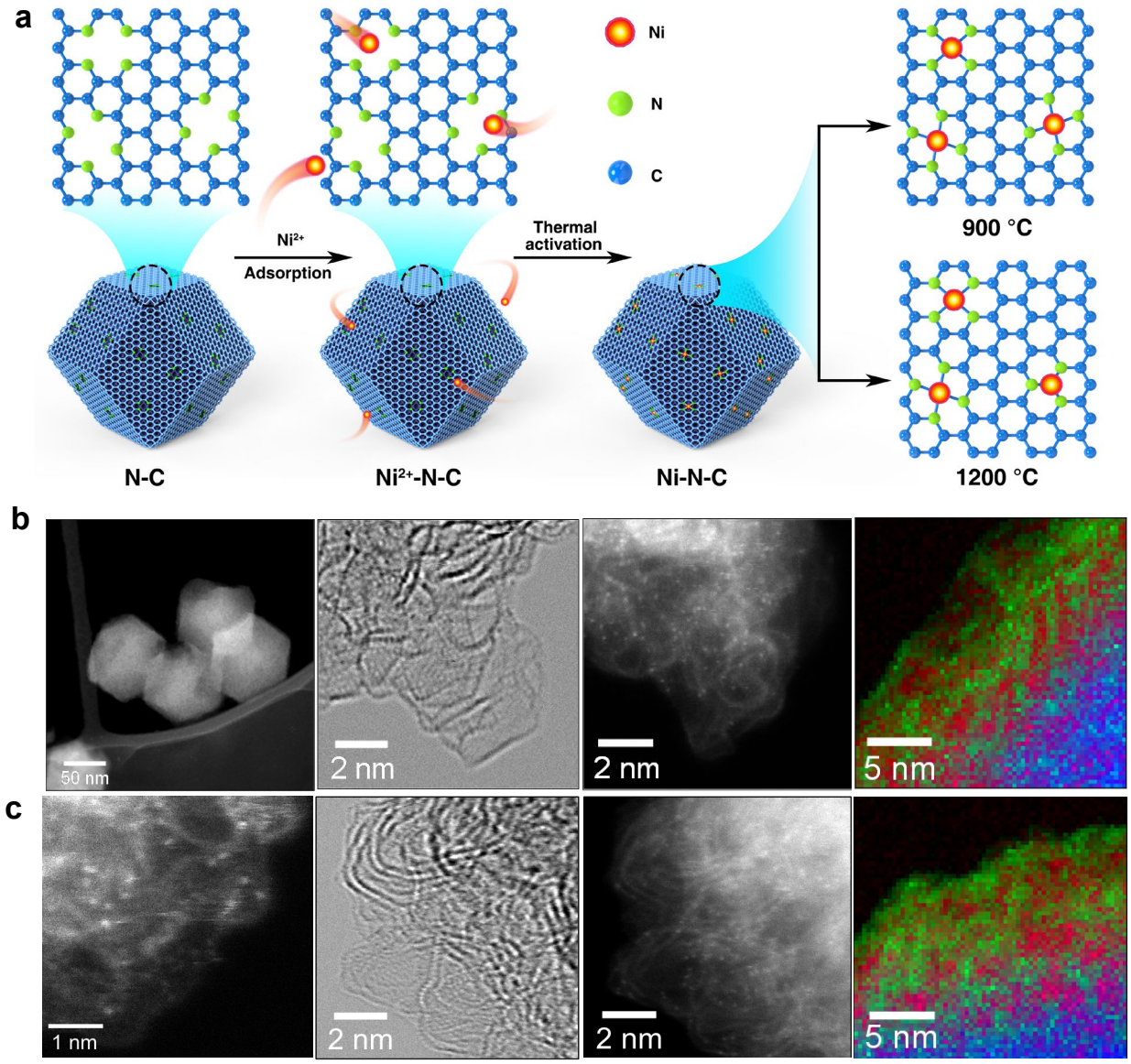

Figure 1. (a) Synthesis scheme for the Ni-N-C catalysts by using a nitrogen-doped carbon host to absorb Ni ions followed by thermalo activation at different temperatures to tune the Ni-N bond structurs and establish the structure-property correlations. Morphology characterization of Ni-N-C at a thermal activation of 900 °C. Various electron microscopy to study the Ni-N-C catalyst from 900ºC (b) and 1200 ºC (c). The BF-STEM images study the nanoscape carbon structure. HAADF-STEM images demonstrated the atomically dispersed nature of the metal sites. Carbon K-edge EELS orientational mapping by multivariate curve resolution (MCR), in which red indicates domains with graphitic sheets oriented perpendicularly to the beam direction, while green indicates domains with sheets parallel to the beam.

Electron microscopy was also utilized to complement the hypothesis from the BET analysis. As shown in Figure S8, Ni clusters on the Ni(II) ion adsorbed N-C samples can be seen even after thermal activation at 400 °C. Upon 900°C, a high density of bright spots can be identified that correspond to N-coordinated atomic Ni sites as confirmed by HAADF-STEM (Figure 1b) and electron energy-loss spectroscopy (EELS) point spectra (Figure 2a). The juxtaposed elemental mapping for the Ni-N-C catalysts activated at 400, 900, and 1200°C shown in Figures 2b-d evidence the transformation of oxide clusters (at 400°C) into homogeneously and atomically dispersed single Ni sites (at above 900°C).

X-ray photoelectron spectroscopy (XPS) and X-ray absorption spectroscopy (XAS) were used to verify the atomically-dispersed structure of the Ni sites and understand their coordination environment. As shown in Figure 3a, the high-resolution XPS for the N 1s spectra can be deconvoluted to oxide-bound (~404.0 eV), graphitic (~402.2 eV), Ni-N_x (~399.5 eV), and

pyridinic (398.2 eV) species, respectively. An apparent attenuation of the Ni-N_x peaks can be seen with the increasing of temperature, suggesting their evaporation with increased thermal energy supplied, which is in line with the decrease of the overall Ni content from 1.1 at.% at 400 °C to 0.3 at.% at 1200 °C (Figures S9, S10 and Table S1). The existence of low-valent state Ni-N_x moieties (between the valence of 0 to +2) can be theorized from the N 1s (~399.5 eV) and Ni 2p (~855.0 eV) peaks, in which a slight shift (~0.2 eV) to lower binding energy suggests a reduction in valency as temperature increases from 400 to 1200°C. Additionally, previous reports found that the pyridinic N is most likely coordinated with metals to form M-N_4 sites derived from ZIF-8 precursors.[40, 42] Also, the Ni-N-C sample activated at 900 °C has the highest total and pyridinic nitrogen content of the studied catalysts at different activation temperature. The ratio of N to Ni in the Ni-N-C-900 is approximately 4, which is higher than those of 3.6/1 in the Ni-N-C-1000 and 2.8 in the Ni-N-C-1200 catalysts. Thus, the loss of N atoms from atomic NiN_4 sites is likely to form NiN_3 sites at thermal activation temperature > 1000°C.

With an increase of adsorption amount of Ni^{2+} (*i.e.*, 10, 50 and 70 μL of 50 mg/l $Ni(NO_3)_2$ solution), both overall surface Ni content (i.e., 0.2, 0.5 and 0.6 at.%, respectively in the Ni XPS) and the Ni-N_x moieties (i.e., 0.69, 0.78 and 0.92 at.%, respectively in the N XPS) are raised, evidenced from Figure S11 and Table S2. When different sizes of ZIF-8-derived N-C host were employed to design single Ni site catalysts, higher concentrations of both Ni and N were found for the medium 120 nm-sized particles (Figure S12 and Table S3). This is consistent with the previous finding that an optimally sized carbon host improves the active metal site density *via* exposing dominant surface micropores and nitrogen dopants to anchor them.[27]

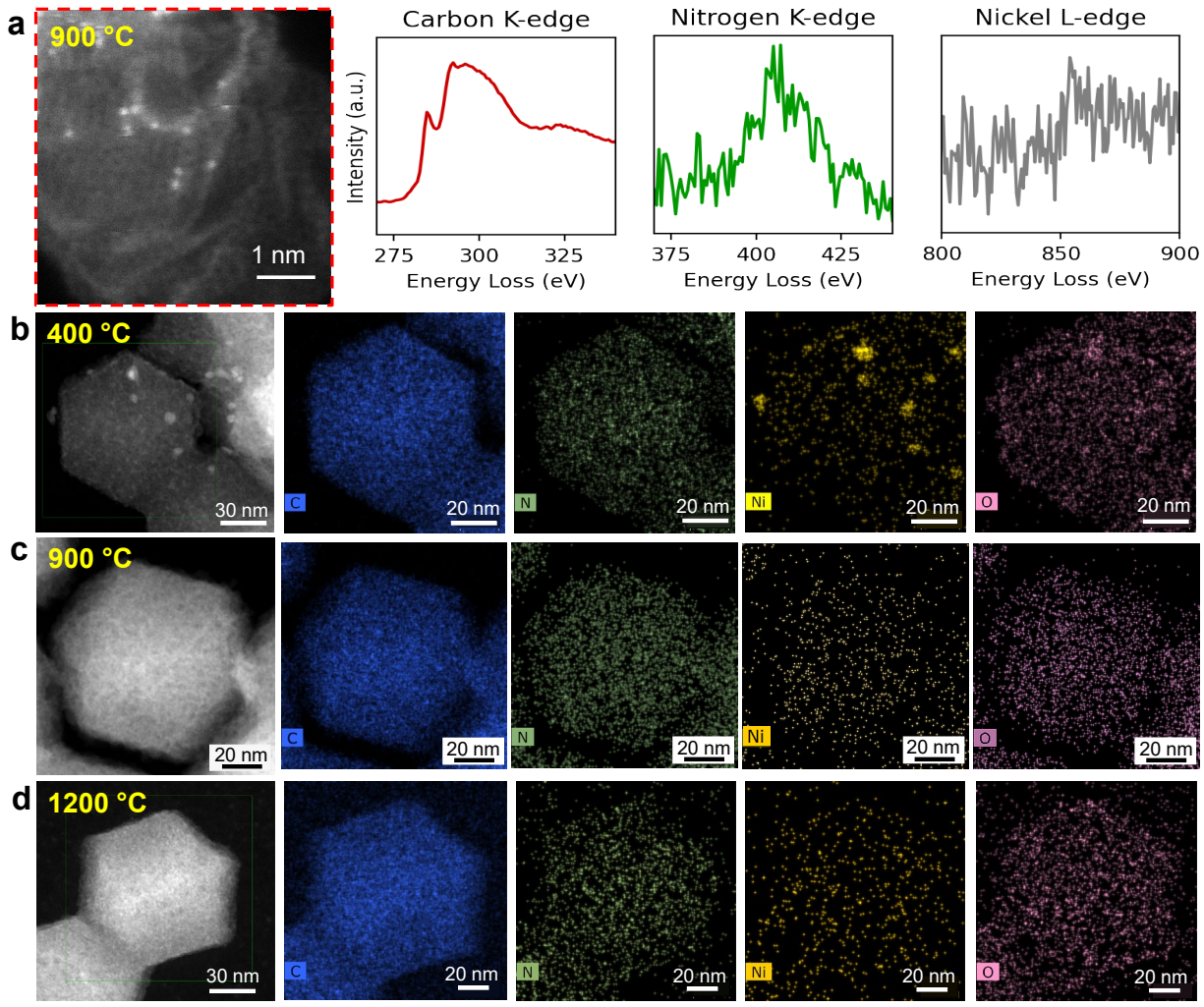

Figure 2. (a) HAADF-STEM image of Ni-N-C activated at 900 °C and the corresponding EELS point spectra, acquired and averaged over multiple metal atoms such as those in the first panel. (b-d) HAADF-STEM and the corresponding EDS element mapping showing the homogeneous distribution of C, N, and Ni atoms on the surface for Ni-N-C with 900 °C and 1200 °C as compared to noticeable metallic clusters on Ni-N-C with 400 °C thermal activations. Temperature labels indicate activation temperature; samples were characterized at room temperature.

Figure 3b shows a pre-edge at ~8340 eV of X-ray absorption near edge structure (XANES) for all samples, indicating a partial oxidation state induced by free-electron sharing between Ni

and either C, N, or O. Due to the lack of Ni-C signal observed in XPS, C-coordination could be excluded during the XAS results fitting. Moreover, there is a singular peak at ~1.4 Å in the Fourier-transformed extended X-ray absorption fine structure (FT-EXAFS) (Figure 3c and S13, and the absence of metallic Ni-Ni scattering substantiate the atomically-dispersed nature of single Ni sites.[43, 44] Thus, the EELS analysis (Figure 2a) coupled with the XAS fitting strongly suggests the coordination between single Ni sites and N ligands. Some possible Ni-O species could exist at a lower temperature of 400 °C, also supported by EDS element mapping (Figure 2). As the heating temperature increases to 900 °C, the pre-edge peak around 8340 eV becomes more pronounced. The peak position moves from 8350 eV to 8360 eV, which shows more similarity to the XANES of NiPc with more Ni-N coordination and loss of Ni-O species. In addition, the EXAFS fitting results also suggest the missing of Ni-O coordination at 900 °C (Table S5). The Ni-N bond length for Ni-N-C catalysts at 400 and 900ºC are 1.85 and 1.62 Å, respectively. Significantly, a shortened Ni-N bond and increased Ni-N coordination number (4.06) at 900 ºC significantly improve catalytic properties (Figure S14, S15, and Table S4, S5). Upon heating to 1200 °C, the Ni-N coordination number was reduced to 3.54, suggesting a final intermixed state of Ni-N_3-C and Ni-N_4-C in the sample. The newly formed Ni-N_3 moieties in the sample could give rise to a change for its intrinsic activity due to the changed coordination environment of Ni atoms, which is discussed in the following discussion. Figure 3d illustrates the evolution of the active sites with varying activation temperatures, starting from relatively uncompressed and flat graphene layer dotted with Ni clusters to slightly crumpled and wrinkled graphene layer filled with atomically-dispersed Ni sites with short Ni-N bonds. The Ni clusters were gradually converted into highly active atomically-dispersed Ni-N_4 sites. Further increasing the thermal activation (*i.e.*, 1200°C)

ultimately leads to a shrinkage of the graphene layer with reduced coordination numbers of single Ni sites (*e.g.*, NiN_3) due to the possible evaporative loss of various N-species.

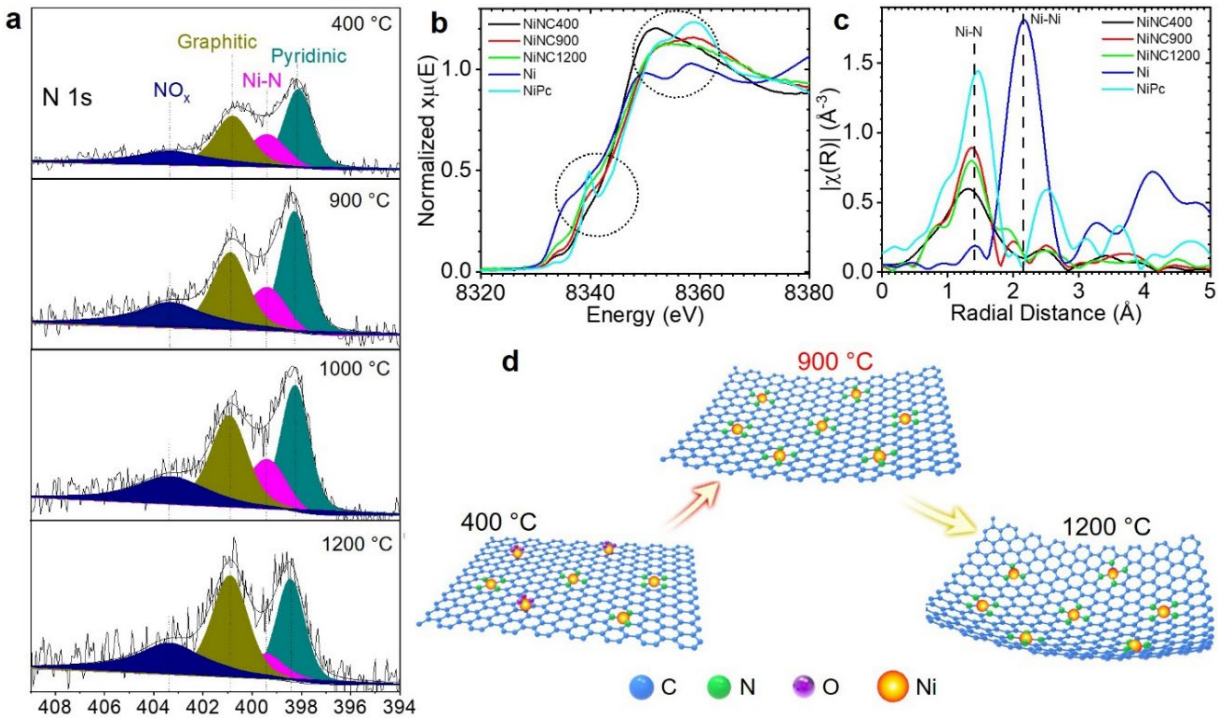

Figure 3. (a) Deconvoluted N 1s spectra of Ni-N-C activated at different temperatures. (b) Ex-situ Ni K-edge XANES spectra of Ni-N-C activated at different temperatures with various reference samples as a comparison for different oxidation states (Ni and Ni phthalocyanine). (c) Fourier-transformed EXAFS spectra in R-space for all samples from (b). (d) Schematic of the evolution of the Ni-N-C sites with increasing thermal activation temperatures.

2.2 Electrochemical reduction of CO_2 to CO

2.2.1 CO_2RR catalytic properties by using H-cell

The defined Ni-N-C catalyst model systems designed in this work allow us to control carbon particle size, Ni content, and Ni-N bond structures separately, which could exclusively correlate

to their corresponding catalytic activity and selectivity for CO_2 reduction to CO. At first, these Ni-N-C catalysts were evaluated in a 0.5 M CO_2-saturated $KHCO_3$ electrolyte using an H-cell with stirring to minimize mass transfer limitation.[45] Without any active metal sites present,[27] the CO_2RR performance, particularly the CO current density (J_{CO}), is negligible, highlighting that the performance uniquely originated from the active Ni sites. An online gas chromatograph (GC) calibrated with a standard gas of ~500 ppm of CO, H_2, and CH_4 (Figure S16) was used for FE determination, in which CO and H_2 were almost exclusively detected with only trace amounts of CH_4 present. It should be noted that the unique isotopic CO_2 experiments are desirable to exclude the possibility that the measured CO is from carbon catalysts rather than CO2RR. Janaky *et al*.,[46] have carried out isotopic labeling experiments based on nitrogen-doped porous carbon electrodes to elucidate the electrochemical CO_2RR mechanisms. By using nonequilibrated solutions of selectively labeled initial carbon sources (*i.e*., $^{13}CO_2$ and $H^{13}CO_3^-$), bicarbonate anion was identified as the predominant source of the CO reduction product. In addition, from the thermodynamic point of view, carbon oxidation to form CO_2 or CO should only occur when the potentials are higher than the standard potential, i.e., 0.207 V. In contrast, the CO_2RR is conducted at a negative potential from -0.1 to -1.0 V vs. RHE. Therefore, the possibility of carbon oxidation to generate CO during the CO_2RR is negligible.

The linear sweep voltammetry (LSV) curves of the Ni-N-C catalyst in 0.5 M $KHCO_3$ display significantly higher current density when bubbled with CO_2, outperforming Ar (Figure S17). This generally indicates an obvious occurrence of CO_2 reduction. Firstly, we investigated the particle size (*e.g*., 40, 120, and 2000 nm) effect of N-C hosts on the CO_2RR performance of the obtained Ni-N-C catalysts with the same Ni ion adsorption and thermal activation (Figure 4a, b). The N-C host with an optimal particle size (*e.g*., 120 nm) could host the maximum active Ni site content,

showing the highest catalytic activity (Table S3). For example, the J_{CO} of the catalyst from 120 nm N-C host is 92.1 mA cm^{-2} at –0.9 V *vs.* RHE, higher than that of the 40 nm (67.2 mA cm^{-2}) and 2000 nm (39.6 mA cm^{-2}). Secondly, for the control of the Ni content, a specific N-C host (i.e., 120 nm) was used to adsorb Ni ion solution (50 mg mL^{-1}) with various amounts (*e.g.*, 10, 30, 50, and 70 μL) (Figures 4c, d). Although the CO FEs of these catalysts only show small changes (Figure 4c), their CO partial current densities greatly depend on adsorption content. For example, the Ni-N-C catalyst from 50 μL ion adsorption presents the highest J_{CO} of 92.1 mA cm^{-2} at –0.9 V *vs.* RHE (Figure 4d). Finally, the optimal N-C host (*i.e.*, 120 nm) and Ni ion adsorption content (*i.e.*, 50 μL of the Ni nitrate solution) were selected to solely study the correlation between catalytic properties and Ni–N bond structures tunable by varying the subsequent thermal activation temperatures from room temperature to 1200 °C. Figures 4e and 4f show the CO FE and J_{CO}, respectively, of Ni-N-C catalysts thermally activated at different temperatures (T = 25, 400, 800, 900, 1000, and 1200 °C). The CO_2RR activity is almost negligible for the sample without thermal activation. With a mild activation at 400 °C, the CO_2RR activity is evidenced with a CO FE of 88% and J_{CO} of 43.7 mA cm^{-2}, and is much higher than that of the Fe-N-C catalyst thermally-activated at 400 °C (CO FE < 10% and J_{CO} < 6.0 mA cm^{-2}).[27] When the thermal temperature was further increased up to 900 °C, maximal CO_2RR performance (CO FE of 92% and J_{CO} of 92.1 mA cm^{-2}) was achieved. Higher temperatures (T > 900 °C) led to a decline in activity to half of the CO_2RR rate (current density) activated at 900 °C (Figures 4e and 4f), which is likely due to evaporative loss of active sites, including N ligands and single Ni sites. Despite the reduced activity (J_{CO} of 46.5 mA cm^{-2}), the highest CO FE of 95% is obtained at 1200°C, likely due to an enhanced intrinsic activity originating from the increased strain and the reduced Ni-N coordination number. Additionally, the high CO_2RR activity of the Ni-N-C catalysts was further demonstrated by a

loading control (*i.e.*, 0.1, 0.2, 0.4, 0.8, and 1.0 mgcm^{-2}) on the best-performing Ni-N-C activated at 900 °C in a 0.5 M $KHCO_3$ aqueous solution (Figure S18). For example, the current density at 0.9 V *vs*. RHE was increased from 59.1 (0.1 mgcm^{-2}) to 92.1 mA cm^{-2} (0.8 mgcm^{-2}). Further increasing loading causes marginal improvement of CO_2RR activity.

Even in lower molarity of 0.1 M $KHCO_3$, the performance of the best performing Ni-N-C catalyst at –0.9 V *vs.* RHE (Figure S19) is twice that of Fe-N-C prepared using a similar method.[27] At the same time, small changes in the CO selectivity may be attributed to the different metal active sites. Notably, a high mass-normalized turn-over frequency approaching 5500 h^{-1} was obtained with the best-performing Ni-N-C catalyst (Figure S20), outperforming other Ni-N-C catalysts (e.g., <3000 h^{-1})[31, 47-53] and confirming the high intrinsic activity of each Ni site.

The stability of the best performing Ni-N-C catalyst was tested at an overpotential of 490 mV (Figure 4g) for up to 70 hours showing its robust catalytic performance, maintaining above 90.0% of CO FE at the end of the test. Unfortunately, similar to other single metal sites such as Fe-N-C catalysts, a significant decrease in the current density (~50% loss of its initial one) was observed. This phenomenon is repeatedly seen across various M-N-C-based catalysts for the CO_2RR to CO. In the case of Fe-N-C, the degradation can be attributed to the passivation of the more active +3 oxidation state to the less active +2 oxidation state.[23] A similar change of the Ni oxidation state can be inferred for the Ni-N-C, although this needs to be substantiated with *in-situ* XAS data.[44, 54] Overall, the catalytic performance reported in this study represents one of the best Ni-N-C catalysts so far, reaching an impressive 61.1 mA cm^{-2} at a minimal overpotential of 490 mV (Table S6).

2.2.2 CO_2RR activity and selectivity in a flow cell

Although an H-cell is useful for catalyst pre-screening purposes, the CO_2RR is severely limited by the mass-transport limitation of CO_2 due to its low solubility in most aqueous solutions.[55, 56] To

further demonstrate the high activity and selectivity of the Ni-N-C catalyst towards CO_2 to CO reduction at a scaled-up industrial level, we thus designed a flow cell electrolyzer. In a typical procedure, 2.0 mg cm^{-2} of catalyst was carefully spray-coated onto a 0.5 × 0.5 cm^2 carbon paper gas-diffusion electrode (GDE) (Sigracet 38 BC). Sandwiched between two compartments of cathode Ni-N-C-900 GDE) and anode catalyst (Ni foam) is a piece of an anion-exchange membrane (Fumasep FAA-3-50). 1.0 M KOH solution was used as both the catholyte and anolyte by continuously circulating at approximately 10 mL min^{-1} using a dual pump-head peristaltic pump. A CO_2 flow at 55.0 mL min^{-1} is fed to the cathode throughout the test. The testing was conducted using a constant-current mode, and the cell voltages (average after 20 mins of run) were recorded with iR correction using a Squidstat potentiostat.

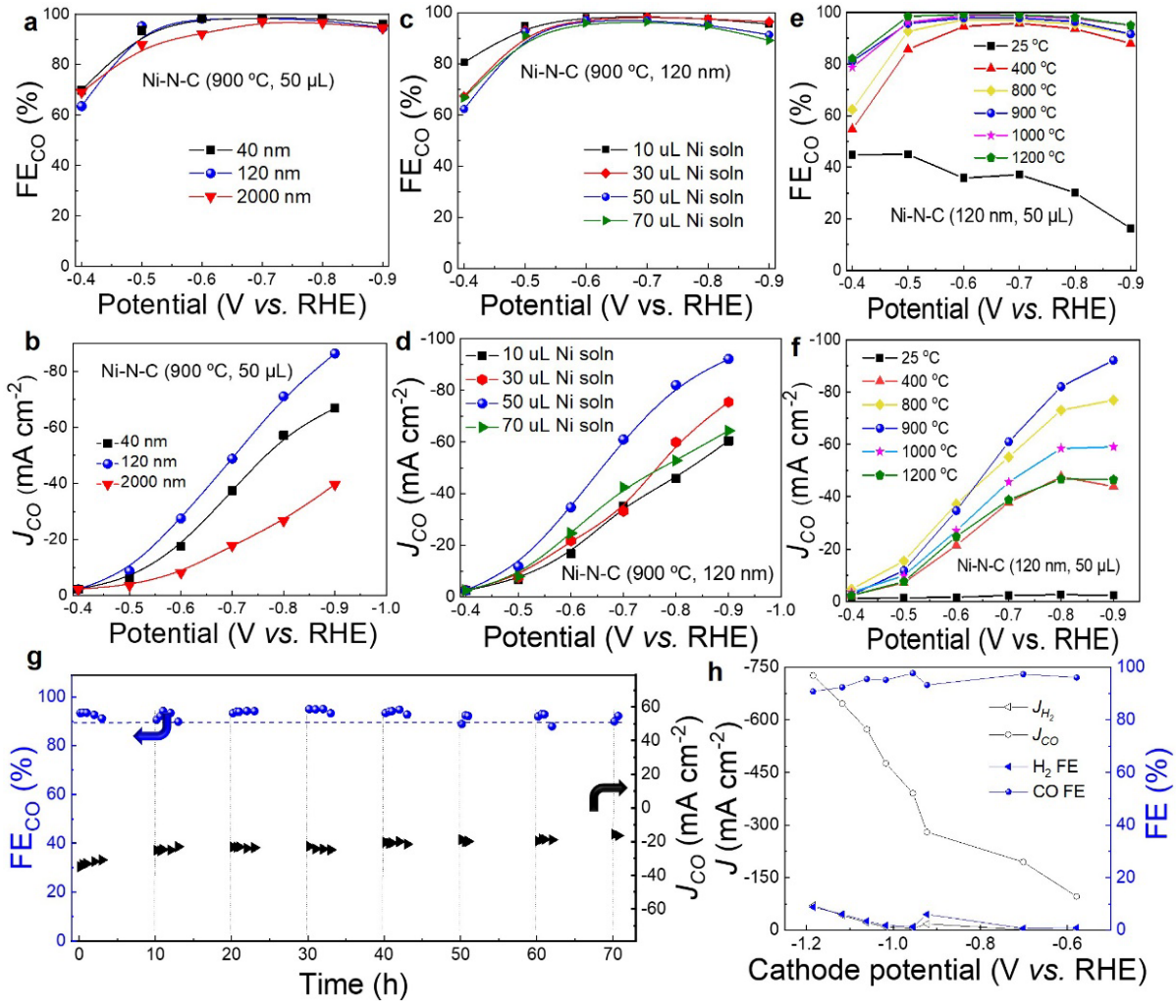

Figure 4. Electrochemical performance of Ni-N-C in 0.5 M $KHCO_3$ solution with catalysts loading of 0.8 mg cm^{-2} on 0.5×0.5 cm^2 carbon paper. (a) CO FEs and (b) J_{CO} of Ni-N-C with different sizes of N-C host. (c) CO FEs and (d) J_{CO} of Ni-N-C with varying volumes of Ni soln. (e) CO FEs and (f) J_{CO} of Ni-N-C thermally activated at various temperatures. (d) Stability of the Ni-N-C catalyst thermally activated at 900 ° C at a constant potential of –0.6 V vs. RHE. (e) Flow cell electrolyzer performance of the Ni-N-C activated at 900 °C in 1.0 M KOH with loading of 2.0 mg cm^{-2}.

As shown in Figure 4h, under a wide cell voltage testing condition, the Ni-N-C catalyst maintained above 90% selectivity for CO generation. Even at high J_{CO} of 195, 391, and 726 mA cm^{-2}, the CO FEs of ~97, 98, and 91% were obtained at cathode potentials of –0.70, -0.96, and –1.18 V, respectively. Notably, the flow cell CO_2RR performance of the best performing Ni-N-C-900 catalyst is superior to many reported catalysts, including both the noble-metal Ag- (*e.g.*, J_{CO}: 275 mA cm^{-2} at –1.00 V)[57] and Au-based catalysts (e.g., J_{CO}: 158 mA cm^{-2} at –0.55 V)[58], as well as other M-N-C catalysts (*e.g.*, CoPc-CN/CNT[59], J_{CO}: ~31 mA cm^{-2} at –0.67 V and NiSA/PCFE[60], J_{CO}: 337 mA cm^{-2} at –1.20 V), see Table S7. Therefore, the remarkable CO_2RR activity and CO selectivity of the optimal Ni-N-C catalyst have been confirmed in both H cell and flow cell tests.

2.3 Theoretical understanding of NiN_x active sites

We further performed first-principles density functional theory (DFT) calculations to elucidate the impact of the increased Ni-N strain induced by thermal wrinkling of graphene and its potential correlation with CO_2RR performance. The XAS experimental results revealed that the shortened Ni-N bonds in the active site moiety (Table S5) are related to the structural distortion in graphene (*i.e.*, carbon plane) under elevated thermal activation temperatures. Graphene layers are known to exhibit a negative thermal expansion coefficient, namely, contraction at high temperatures.[61] Consequently, we modeled the structural distortion in a graphene layer by applying compressive strain to shorten the Ni-N bonds in the NiN_4 active site, consistent with our XAS fitting results. Specifically, the degree of structural distortion was quantitatively studied using the percentage of Ni-N bond shortening.

Since the best-performing Ni-N-C catalyst was activated at 900 °C with a coordination structure of one Ni chelated with N, the DFT study was mainly focused on this particular coordination environment. Here, three NiN_x sites were modeled, including a fully embedded NiN_4

site (Figure 5a), an edge-to-edge Ni-N_{2+2} site (Figure S21), and a Ni-N_3 site (Figure 5b), aiming to correlate their CO_2RR activity and selectivity with the coordination number and local structures. The fully embedded Ni-N_4 site consists of a Ni site in a double-vacancy site with four neighboring pyridinic N atoms in a planar graphene layer.[28] The edge-to-edge Ni-N_{2+2} site was modeled by bridging two N-doped graphene edges with a Ni site. The Ni-N_4 site strained by –2% (Figure 5a) exhibits a nonplanar configuration, whereas the –1.5% compressively strained Ni-N_{2+2} site (Figure S21a) still maintains a planar configuration.

Subsequently, we calculated the free energy evolution for the CO_2RR via a coupled proton-electron transfer reaction pathway on both strained and unstrained Ni-N_4 and Ni-N_{2+2} sites. The stable adsorptions of *COOH and *CO on the Ni-N_4 and Ni-N_{2+2} sites are shown in Figures S22 and S23, respectively. The adsorption of *COOH was calculated to be the potential determining step (PDS) for the CO_2RR on all the sites, as it requires the largest positive free energy change along the reaction pathway. The electrode potential needed to overcome such positive free energy change in PDS is defined as the limiting potential for the CO_2RR ($U_{L(CO2RR)}$). The value of $U_{L(CO2RR)}$ on the NiN_4 sites (Figure 5c) was predicted to be –1.50 V on the unstrained and –1.40 V on –2% strained sites, respectively, predicting higher CO_2RR activity on the NiN_4 sites with compressive strain.

Furthermore, as shown in Figure S21b, the –1.5% strained NiN_{2+2} site also shows a more positive value of $U_{L(CO2RR)}$ (–1.04 V) than the unstrained one (–1.16 V for $U_{L(CO2RR)}$). Moreover, UL(CO2RR) values of both unstrained and strained NiN_{2+2} sites are at least 0.34 V more positive than those of the NiN_4 sites. Thus, the NiN_{2+2} sites are more active than the NiN_4 sites, agreeing with the conclusions of previous studies that the Ni-N_{2+2}-C_8 site with dangling carbon bonds is thermodynamically and kinetically active for the CO_2RR.[14, 28]

On the other hand, strained Ni-N bonds cause a negative impact on the CO_2RR. As shown in the predicted free energy evolution of CO_2RR on NiN_4 (Figure 5d) and NiN_{2+2} sites (Figure S21c), a compressive strain also leads to stronger *CO adsorption and correspondingly a more positive value of free energy change for the *CO desorption. For example, the –1.5% strained NiN_{2+2} site exhibits a more positive free energy change by 0.17 eV for the *CO desorption (i.e., stronger adsorption) than the unstrained one. However, the required free energy change in this desorption step (0.29 eV) on the compressively strained site is still surmountable. Therefore, the negative impact of strained Ni-N bonds on the *CO desorption is negligible compared to its positive role in thermodynamically facilitating the CO_2 to CO reduction.

Furthermore, the CO_2RR selectivity on the NiN_4 and NiN_{2+2} sites was evaluated by comparing their activity for the CO_2RR and the HER. The free energy evolution of HER was calculated by considering the stable adsorption of *H on NiN_4 and NiN_{2+2} sites (Figure S22, S23). The difference in the limiting potential of CO_2RR and HER ($U_{L(CO2RR)} - U_{L(HER)}$) was computed to represent the CO_2RR selectivity. A more positive value indicates better CO_2RR selectivity. As shown in Figure S24, the value of $U_{L(CO2RR)} - U_{L(HER)}$ is positive on all sites, which indicates HER is suppressed on all these Ni sites. The compressive strain in NiN_4 and NiN_{2+2} sites leads to an additional increase of the $U_{L(CO2RR)} - U_{L(HER)}$, further enhancing the selectivity. Therefore, our DFT results revealed that shortening the Ni-N bonds in compressively strained NiN_4 and NiN_{2+2} sites could enhance the CO_2RR activity and selectivity pyrolyzed Ni-N-C catalysts.

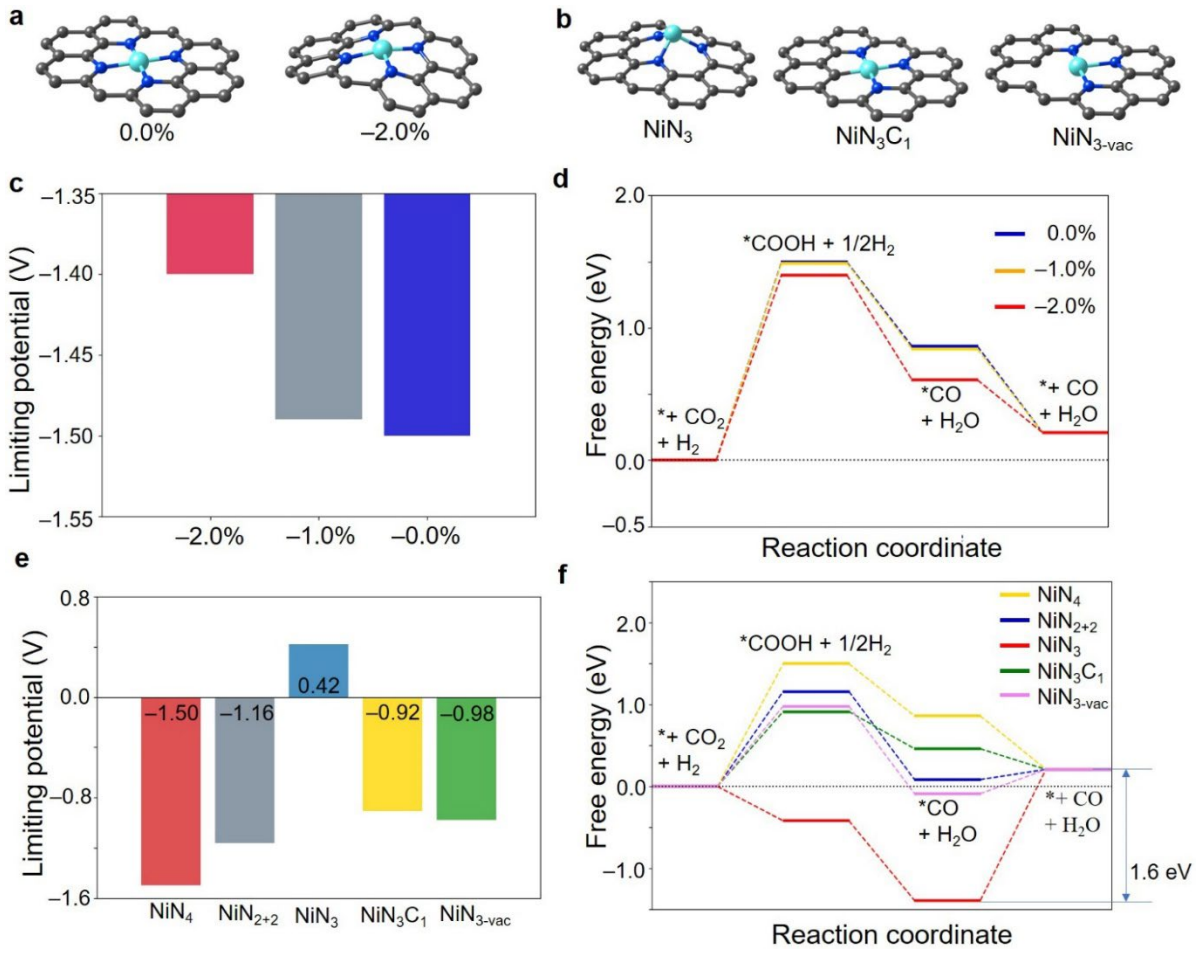

Figure 5. (a) Atomic structures of unstrained and –2% compressively strained Ni-N_4 sites. (b) Atomic structures of Ni-N_3, Ni-N_3C_1, and $NiN_{3\text{-vac}}$ sites. The gray, blue, and cyan balls represent C, N, and Ni atoms, respectively. (c) Predicted limiting the potential of CO_2RR on Ni-N_4 sites with various strains and (d) predicted free energy evolution of CO_2RR on Ni-N_4 sites with various strains. (e) Predicted limiting potential of the CO_2RR on different Ni-based sites and (f) different Ni-based sites under the electrode potential of 0 V.

Ni-N-C catalyst thermally activated at 1200 °C displays the highest CO_2RR selectivity but a lowered activity (Figures 4b, c). Thus, we further performed the DFT calculations on a NiN_3 structure to elucidate the experimental result. Due to an apparent nitrogen loss (Table S1) and the

change of Ni-N coordination number to ~3.54 (Table S5) in the Ni-N-C-1200 catalyst, a possible mixed structure of NiN_3 and NiN_4 active site in the catalyst is very likely. Here, three possible NiN_3 site configurations were studied: NiN3, NiN3C1, and NiN3-vac (Figure 5b). The calculated $U_{L(CO2RR)}$ values on these sites are compared with those on unstrained NiN_4 and NiN_{2+2} sites in Figure 5e. All three sites show stronger *COOH adsorption with more positive $U_{L(CO2RR)}$ than NiN_4 sites, suggesting enhanced CO_2RR intrinsic activity. The predicted free energy evolution for CO_2RR (Figure 5f) shows much stronger *CO adsorption on the NiN_3 site than that on other modeled sites, which requires 1.6 eV free energy change for *CO desorption. In contrast, the *CO desorption on the NiN_3C_1 site shows a negative free energy change (–0.25 eV) and a surmountable free energy change on the $NiN_{3\text{-vac}}$ site (0.30 eV). We also examined the CO_2RR selectivity on these sites (Figure S25). The *H adsorption was predicted to be weaker on them than NiN_4 sites (Figure S25a). The $NiN_{3\text{-vac}}$ site is the only one with a positive $U_{L(CO2RR)} - U_{L(HER)}$ value among the three modeled NiN_3 sites (Figure S25b), which indicates only the $NiN_{3\text{-vac}}$ site could have high CO_2RR selectivity. Also, We conducted DFT calculations to examine the strain effect on the NiN_3 site. The NiN_3 site doped graphene unit cell was compressed to the same degree as the strained NiN_4 site model. The predicted limiting potential of CO2RR only changes from -0.418 V on the unstrained NiN_3 site to -0.421 V on the strained NiN_3 site. The calculated limiting potential difference between CO2RR and HER changes from -0.099 V on the unstrained NiN_3 site to -0.094 V on the strained one. Thus, the change of CO2RR activity and selectivity of the strained NiN_3 site is infinitesimal, comparable with the numerical error in math calculations. Therefore, the compressive strain on the NiN_3 site can cause no change in the CO2RR performance of NiN_3 sites.

In theory, the Ni-N-C activated at 1200°C containing $NiN_{3\text{-vac}}$ sites and strained NiN_{2+2} sites should be the best-performing catalyst. However, such a high-temperature treatment often causes

the loss of active Ni sites, verified from the XPS results decreasing Ni content from 0.5 at% at 900 °C to 0.3 at% at 1200 °C. Breaking the trade-off via innovative synthesis methods and concepts may yield advanced single Ni site catalyst with simultaneously enhanced mass activity and intrinsic activity for the CO_2RR.

3. Conclusion

In this work, we carefully deconvoluted multiple extrinsic and intrinsic factors critical in designing Ni-N-C catalysts for the CO_2RR. Using a unique model catalyst system, vital factors such as carbon particle sizes, Ni content, and Ni-N bond structures and coordination could be well-controlled and solely correlated to measured catalytic properties. Most adsorbed Ni ions initially existed as oxide clusters, which were transformed into N-coordinated sites with thermal activation above 900 °C. As for the external factors, active site accessibility is crucial due to the microporous nature of the ZIF-8 derived carbon host. Although the same amount of Ni was doped into the carbon hosts with different sizes, the final surface-level Ni accessible and detectable by the XPS differed greatly. During the formation of NiN_x sites, the available N and defect sites to anchor the Ni ions are also essential. While the amount of Ni introduced correlates to the density of Ni-N sites, much of the Ni ended up as CO_2RR-inactive aggregates.

A significant finding from this work is the impacts of the different thermal activation temperatures on the intrinsic activity and selectivity of active sites toward the CO2RR. In particular, this work elucidated the structural evolution of the atomically dispersed and nitrogen coordinated single Ni sites during thermal activation from small Ni-clusters, NiN_4 moieties, to NiN_3 with decreased N-coordination numbers and increased Ni-N bond strain at elevated activation temperatures. Due to the contraction of the superficial graphene layers where the Ni-N-C sites reside, the Ni-N bonds are shortened with increased thermal activation temperatures. The

coordination environment is also affected due to evaporative loss of the N-species. The DFT calculations revealed that the compaction of the Ni-N bonds could positively affect the CO_2RR, both in the case of in-plane embedded NiN_4 and the more-active edge-located NiN_{2+2} sites. The NiN_3 sites with optimal local structures formed at extremely high temperatures (*i.e.*, 1200ºC) could be more intrinsically active and selective to CO, but often suffered from significantly reduced active site density. Therefore, novel synthetic methods are demanded to mitigate active Ni site evaporation at high heating temperatures, ensuring dense single Ni sites with an optimal Ni-N strain and low N coordination number for advanced Ni-N-C catalysts.

Through the intensive engineering of the extrinsic particle size and metal content along with intrinsic Ni-N bond structures in the catalyst, the best-performing Ni-N-C catalyst generated an encouraging CO_2RR activity that represents one of the best CO_2 to CO catalysts, approaching 92.3 mA cm^{-2} at –0.9 V *vs.* RHE in an H-cell test for CO generation. Notably, the same catalyst in a flow cell AEM electrolyzer can generate J_{CO} up to 726 mA cm^{-2} while maintaining CO FE above 90%.

Conflicts of interest

The authors do not have a conflict of interest

Acknowledgments

G. Wu and G.F. Wang acknowledge the support for a collaborative project from the U.S. National Science Foundation (CBET-1804326 and 1804534). The energy-dispersive X-ray spectroscopy and the corresponding scanning transmission electron microscopy were conducted at the Center for Functional Nanomaterials at Brookhaven National Laboratory (under contract No. DE-SC0012704). The high-resolution scanning transmission electron microscopy and electron energy-

loss spectroscopy were conducted the Center for Nanophase Materials Sciences, which is a U.S. DOE Office of Science User Facility. Z. Feng thanks the U.S. National Science Foundation (NNCI-2025489). XAS measurements were performed at beamline 12-BM at the Advanced Photon Source, a User Facility operated by Argonne National Laboratory under Contract No. DE-AC02-06CH11357 (Z.F.). DND-CAT is supported through E. I. duPont de Nemours & Co., Northwestern University, and The Dow Chemical Company. Y. Li. thanks the Natural Science Foundation of Jiangsu Province (BK20210769).

References

1. S. Hernández, M. Amin Farkhondehfal, F. Sastre, M. Makkee, G. Saracco and N. Russo, *Green Chem.*, 2017, **19**, 2326–2346.
2. Y. Li, H. Wang, C. Priest, S. Li, P. Xu and G. Wu, *Adv. Mater.*, 2021, **33**, 2000381.
3. J. Li, H. Zhang, W. Samarakoon, W. Shan, D. A. Cullen, S. Karakalos, M. Chen, D. Gu, K. L. More, G. Wang, Z. Feng, Z. Wang and G. Wu, *Angew. Chem. Int. Ed.*, 2019, **58**, 18971–18980.
4. M. G. Kibria, J. P. Edwards, C. M. Gabardo, C. T. Dinh, A. Seifitokaldani, D. Sinton and E. H. Sargent, *Adv. Mater.*, 2019, **31**, 1807166.
5. F. Pan and Y. Yang, *Energy Environ. Sci.*, 2020, **13**, 2275–2309.
6. T. Fu and Z. Li, *Chem. Eng. Sci.*, 2015, **135**, 3-20.
7. A. S. Hall, Y. Yoon, A. Wuttig and Y. Surendranath, *J. Am. Chem. Soc.*, 2015, **137**, 14834-14837.
8. D. Gao, H. Zhou, J. Wang, S. Miao, F. Yang, G. Wang, J. Wang and X. Bao, *J. Am. Chem. Soc.*, 2015, **137**, 4288-4291.
9. Z. L. Wang, C. L. Li and Y. Yamauchi, *Nano Today*, 2016, **11**, 373-391.
10. T. Liu, P. Zhao, X. Hua, W. Luo, S. Chen and G. Cheng, *J. Mater. Chem. A*, 2016, **4**, 11357-11364.
11. A. S. Varela, N. R. Sahraie, J. Steinberg, W. Ju, H. S. Oh and P. Strasser, *Angew. Chem. Int. Ed.*, 2015, **54**, 10758-10762.
12. A. S. Varela, N. Ranjbar Sahraie, J. Steinberg, W. Ju, H.-S. Oh and P. Strasser, *Angew. Chem. Int. Ed.*, 2015, **54**, 10758-10762.
13. X. Li, S. Xi, L. Sun, S. Dou, Z. Huang, T. Su and X. Wang, *Adv. Sci.*, 2020, **7**, 2001545.

14. F. Pan, H. Zhang, K. Liu, D. Cullen, K. More, M. Wang, Z. Feng, G. Wang, G. Wu and Y. Li, *ACS Catal.*, 2018, **8**, 3116–3122.
15. Y. Zhu, J. Sokolowski, X. Song, Y. He, Y. Mei and G. Wu, *Adv. Energy Mater.*, 2020, **10**, 1902844.
16. Q. Shi, S. Hwang, H. Yang, F. Ismail, D. Su, D. Higgins and G. Wu, *Mater. Today*, 2020, **37**, 93-111.
17. Q. Shi, Y. He, X. Bai, M. Wang, D. A. Cullen, M. Lucero, X. Zhao, K. L. More, H. Zhou, Z. Feng, Y. Liu and G. Wu, *Energy Environ. Sci.*, 2020, **13**, 3544-3555.
18. Y. He, Q. Shi, W. Shan, X. Li, A. J. Kropf, E. C. Wegener, J. Wright, S. Karakalos, D. Su, D. A. Cullen, G. Wang, D. J. Myers and G. Wu, *Angew. Chem. Int. Ed.*, 2021, **60**, 9516-9526.
19. X. X. Wang, M. T. Swihart and G. Wu, *Nature Catalysis*, 2019, **2**, 578-589.
20. Y. He, S. Liu, C. Priest, Q. Shi and G. Wu, *Chemical Society Reviews*, 2020, **49**, 3484-3524.
21. X. Li, S. Tang, S. Dou, H. J. Fan, T. S. Choksi and X. Wang, *Advanced Materials*, **n/a**, 2104891.
22. Y. He and G. Wu, *Acc. Mater. Res.*, 2022, **3**, 224-236.
23. Jun Gu, Chia-Shuo Hsu, Lichen Bai, Hao Ming Chen and X. Hu, *Science*, 2019, **364**, 1091–1094.
24. Y. Li, J. Yang, N. Zhao, J. Huang, Y. Zhou, K. Xu and N. Zhao, *Appl. Catal., A*, 2017, **534**, 30–39.
25. L. Lin, H. Li, C. Yan, H. Li, R. Si, M. Li, J. Xiao, G. Wang and X. Bao, *Adv. Mater.*, 2019, **31**, 1903470.

26. Y. Zhu, X. Yang, C. Peng, C. Priest, Y. Mei and G. Wu, *Small*, 2021, **17**, 2005148.

27. N. Mohd Adli, W. Shan, S. Hwang, W. Samarakoon, S. Karakalos, Y. Li, D. A. Cullen, D. Su, Z. Feng, G. Wang and G. Wu, *Angew. Chem. Int. Ed.*, 2021, **60**, 1022–1032.

28. F. Pan, H. Zhang, Z. Liu, D. Cullen, K. Liu, K. More, G. Wu, G. Wang and Y. Li, *J. Mater. Chem. A*, 2019, **7**, 26231–26237.

29. T. Möller, W. Ju, A. Bagger, X. Wang, F. Luo, T. Ngo Thanh, A. S. Varela, J. Rossmeisl and P. Strasser, *Energy Environ. Sci.*, 2019, **12**, 640–647.

30. Y. He, Y. Li, J. Zhang, S. Wang, D. Huang, G. Yang, X. Yi, H. Lin, X. Han, W. Hu, Y. Deng and J. Ye, *Nano Energy*, 2020, **77**, 105010.

31. Yun-Nan Gong, Long Jiao, Yunyang Qian, Chun-Yang Pan, Lirong Zheng, Xuechao Cai, Bo Liu, Shu-Hong Yu and H.-L. Jiang, *Angew. Chem. Int. Ed.*, 2020, **132**, 2727–2731.

32. Y. Zhang, L. Jiao, W. Yang, C. Xie and H. L. Jiang, *Angew. Chem. Int. Ed.*, 2021, **60**, 7607–7611.

33. Q. Fan, P. Hou, C. Choi, T. S. Wu, S. Hong, F. Li, Y. L. Soo, P. Kang, Y. Jung and Z. Sun, *Adv. Energy Mater.*, 2019, **10**, 1903068.

34. C. Zhao, X. Dai, T. Yao, W. Chen, X. Wang, J. Wang, J. Yang, S. Wei, Y. Wu and Y. Li, *J. Am. Chem. Soc.*, 2017, **139**, 8078–8081.

35. S. Mukherjee, X. Yang, W. Shan, W. Samarakoon, S. Karakalos, D. A. Cullen, K. More, M. Wang, Z. Feng, G. Wang and G. Wu, *Small Methods*, 2020, **4**, 1900821.

36. David M. Koshy, Shucheng Chen, Dong Un Lee, Michaela Burke Stevens, Ahmed M. Abdellah, Samuel M. Dull, Gan Chen, Dennis Nordlund, Alessandro Gallo, Christopher Hahn, Drew C. Higgins, Zhenan Bao and T. F. Jaramillo, *Angew. Chem. Int. Ed.*, 2020, **132**, 4072–4079.

37. X. Wang, Y. Wang, X. Sang, W. Zheng, S. Zhang, L. Shuai, B. Yang, Z. Li, J. Chen, L. Lei, N. M. Adli, M. K. H. Leung, M. Qiu, G. Wu and Y. Hou, *Angew. Chem. Int. Ed.*, 2021, **60**, 4192-4198.

38. Y. Li, H. S. Pillai, T. Wang, S. Hwang, Y. Zhao, Z. Qiao, Q. Mu, S. Karakalos, M. Chen, J. Yang, D. Su, H. Xin, Y. Yan and G. Wu, *Energy Environ. Sci.*, 2021, **14**, 1449–1460.

39. Y. He, S. Hwang, D. A. Cullen, M. A. Uddin, L. Langhorst, B. Li, S. Karakalos, A. J. Kropf, E. C. Wegener, J. Sokolowski, M. Chen, D. Myers, D. Su, K. L. More, G. Wang, S. Litster and G. Wu, *Energy Environ. Sci.*, 2019, **12**, 250-260.

40. H. Zhang, H. T. Chung, D. A. Cullen, S. Wagner, U. I. Kramm, K. L. More, P. Zelenay and G. Wu, *Energy Environ. Sci.*, 2019, **12**, 2548–2558.

41. Q. Fan, P. Hou, C. Choi, T.-S. Wu, S. Hong, F. Li, Y.-L. Soo, P. Kang, Y. Jung and Z. Sun, *Adv. Energy Mater.*, 2020, **10**, 1903068.

42. X. Xie, C. He, B. Li, Y. He, D. A. Cullen, E. C. Wegener, A. J. Kropf, U. Martinez, Y. Cheng, M. H. Engelhard, M. E. Bowden, M. Song, T. Lemmon, X. S. Li, Z. Nie, J. Liu, D. J. Myers, P. Zelenay, G. Wang, G. Wu, V. Ramani and Y. Shao, *Nat. Catal.*, 2020, **3**, 1044-1054.

43. M. Wang and Z. Feng, *Curr. Opin. Electrochem.*, 2021, **30**, 100803.

44. M. Wang, L. Arnadottir, Z. J. Xu and Z. Feng, *Nano-Micro Lett.*, 2019, **11**, 47.

45. F. Pan, B. Li, E. Sarnello, S. Hwang, Y. Gang, X. Feng, X. Xiang, N. M. Adli, T. Li, D. Su, G. Wu, G. Wang and Y. Li, *Nano Energy*, 2020, **68**, 104384.

46. D. Hursan and C. Janaky, *ACS Energy Lett.*, 2018, **3**, 722–723.

47. R. Daiyan, X. Zhu, Z. Tong, L. Gong, A. Razmjou, R.-S. Liu, Z. Xia, X. Lu, L. Dai and R. Amal, *Nano Energy*, 2020, **78**, 105213.

48. S. Ji, Y. Chen, X. Wang, Z. Zhang, D. Wang and Y. Li, *Chem. Rev.*, 2020, **120**, 11900-11955.

49. Y.-N. Gong, L. Jiao, Y. Qian, C.-Y. Pan, L. Zheng, X. Cai, B. Liu, S.-H. Yu and H.-L. Jiang, *Angew. Chem. Int. Ed.*, 2020, **59**, 2705-2709.

50. C. Zhao, X. Dai, T. Yao, W. Chen, X. Wang, J. Wang, J. Yang, S. Wei, Y. Wu and Y. Li, *J. Am. Chem. Soc.*, 2017, **139**, 8078-8081.

51. F. Pan, W. Deng, C. Justiniano and Y. Li, *Appl. Catal. B Environ.*, 2018, **226**, 463-472.

52. T. Zhang, X. Han, H. Yang, A. Han, E. Hu, Y. Li, X.-q. Yang, L. Wang, J. Liu and B. Liu, *Angew. Chem. Int. Ed.*, 2020, **59**, 12055-12061.

53. H. B. Yang, S.-F. Hung, S. Liu, K. Yuan, S. Miao, L. Zhang, X. Huang, H.-Y. Wang, W. Cai, R. Chen, J. Gao, X. Yang, W. Chen, Y. Huang, H. M. Chen, C. M. Li, T. Zhang and B. Liu, *Nat. Energy*, 2018, **3**, 140-147.

54. M. Wang, Q. Wa, X. Bai, Z. He, W. S. Samarakoon, Q. Ma, Y. Du, Y. Chen, H. Zhou, Y. Liu, X. Wang and Z. Feng, *JACS Au*, 2021, **1**, 2216–2223.

55. D. M. Weekes, D. A. Salvatore, A. Reyes, A. Huang and C. P. Berlinguette, *Acc. Chem. Res*, 2018, **51**, 910-918.

56. Z. Yin, H. Peng, X. Wei, H. Zhou, J. Gong, M. Huai, L. Xiao, G. Wang, J. Lu and L. Zhuang, *Energy Environ. Sci.*, 2019, **12**, 2455-2462.

57. S. Verma, X. Lu, S. Ma, R. I. Masel and P. J. Kenis, *Phys. Chem. Chem. Phys.*, 2016, **18**, 7075–7084.

58. S. Verma, Y. Hamasaki, C. Kim, W. Huang, S. Lu, H.-R. M. Jhong, A. A. Gewirth, T. Fujigaya, N. Nakashima and P. J. A. Kenis, *ACS Energy Lett.*, 2017, **3**, 193–198.

59. X. Lu, Y. Wu, X. Yuan, L. Huang, Z. Wu, J. Xuan, Y. Wang and H. Wang, *ACS Energy Lett.*, 2018, **3**, 2527–2532.

60. H. Yang, Q. Lin, C. Zhang, X. Yu, Z. Cheng, G. Li, Q. Hu, X. Ren, Q. Zhang, J. Liu and C. He, *Nat. Commun.*, 2020, **11**, 593.

61. M. Pozzo, D. Alfe, P. Lacovig, P. Hofmann, S. Lizzit and A. Baraldi, *Phys. Rev. Lett.*, 2011, **106**, 135501.